

# Efficient Er/O Doped Silicon Photodiodes at Communication Wavelengths by Deep Cooling

Xingyan Zhao, Kaiman Lin, Sai Gao, Huayou Liu, Jiajing He, Xiaoming Wang, Huimin Wen, and Yaping Dan\*

Wide band infrared photodetectors have found a wide range of applications in sensing, communication, and spectral analysis. However, the commonly used infrared photodetectors are based on Ge and III-V semiconductors which are not complementary metal-oxide-semiconductor (CMOS) compatible and therefore have limited applications. There is a huge demand for silicon-based infrared photodetectors due to its low-cost and compatibility with CMOS processes. Nevertheless, the spectral bandwidth of Si photodetectors is limited to wavelengths below 1.1  $\mu\text{m}$ . Several approaches are developed to extend Si photodetection bandwidth to communication wavelengths. Er/O doped Si is a promising approach which, however, suffers from low infrared responsivities at room temperature when the samples are treated with the standard rapid thermal annealing (RTA). In this work, a novel deep cooling process to treat Er/O doped silicon waveguide photodiodes is applied. In comparison with RTA process, the deep cooling process reduces the defect concentration in silicon by two orders of magnitude, resulting in a two-orders-of-magnitude reduction in leakage current density and an enhanced photoresponsivity to 100  $\text{mA W}^{-1}$  at 1510 nm. The 3dB bandwidth of the silicon waveguide photodiode reaches 30 kHz. The device performance can be further improved by optimizing the deep cooling condition and Er/O doping concentration.

## 1. Introduction

During the past decades, wide band infrared (IR) photodetectors have undergone considerable developments and have found applications in various fields from defense, space science, and medical imaging to telecommunication.<sup>[1–7]</sup> The commonly used integrated IR photodetectors are based on epitaxially grown Ge or III-V semiconductor materials.<sup>[8–12]</sup> In compar-

ison, Si-based photodetectors are more cost effective and compatible with complementary metal-oxide-semiconductor (CMOS) processes, and therefore are more competitive in the market.<sup>[13–18]</sup> However, the spectral responses of silicon photodiodes are limited to wavelengths shorter than 1.1  $\mu\text{m}$ , significantly shorter than communication wavelengths ( $\approx 1.55 \mu\text{m}$ ). Approaches have been explored to extend the spectral range of silicon-based photodetectors to communication wavelengths. One involves incorporating chalcogen dopants into Si through picosecond or femtosecond laser irradiation.<sup>[19–22]</sup> Although the room temperature responsivity of 35  $\text{mA W}^{-1}$  at 1550 nm was achieved using this process, it is not suitable for the integrated circuit application due to the complicated laser annealing process and the noncrystalline Si surface formed in the process.<sup>[20,23]</sup> Recently, pulsed laser treatment using nanosecond laser has been reported to form single-crystalline surface on gold ion doped silicon. The resultant Si:Au photodiodes have the maximum room temperature EQE of


$9.3 \times 10^{-5}$  at communication wavelengths.<sup>[24]</sup> Nevertheless, Au is an important detrimental elements to silicon-based devices and therefore incompatible with the CMOS process.<sup>[25,26]</sup>

Although silicon hyper doped with silver was made into photodiodes,<sup>[27]</sup> doping silicon with erbium (often with oxygen)<sup>[28–30]</sup> is particularly interesting for photodetection since Er/O doped silicon can be also potentially made into silicon light sources at communication wavelength.<sup>[31–35]</sup> Traditionally, Er/O doped silicon suffers from Er/O precipitation after standard rapid thermal annealing (RTA), which results in strong nonradiative recombination.<sup>[36–38]</sup> Consequently, the RTA-treated Er/O silicon cannot emit or detect photons at communication wavelengths efficiently at room temperature.<sup>[28,36]</sup> Recently, we employed a deep cooling (DC) process to treat the Er/O implanted silicon.<sup>[31]</sup> The processed samples exhibit a strong photoluminescence at room temperature, two orders of magnitude higher than the samples treated by standard RTA process. In this work, we explore the possibility to use Er/O doped silicon treated by the DC process for high-performance photodetection at communication wavelengths. The samples were first annealed at high-temperature ( $\approx 950^\circ\text{C}$ ) and cooled

Dr. X. Zhao, K. Lin, H. Liu, Dr. J. He, X. Wang, Dr. H. Wen, Dr. Y. Dan  
University of Michigan Shanghai Jiao Tong University Joint Institute  
Shanghai Jiao Tong University  
Shanghai 200240, China  
E-mail: Yaping.dan@sjtu.edu.cn

S. Gao

State Key Laboratory of Advanced Optical Communication Systems  
and Networks Department of Electronic Engineering  
Shanghai Jiao Tong University  
Shanghai 200240, China

 The ORCID identification number(s) for the author(s) of this article can be found under <https://doi.org/10.1002/admt.202100137>.

DOI: 10.1002/admt.202100137

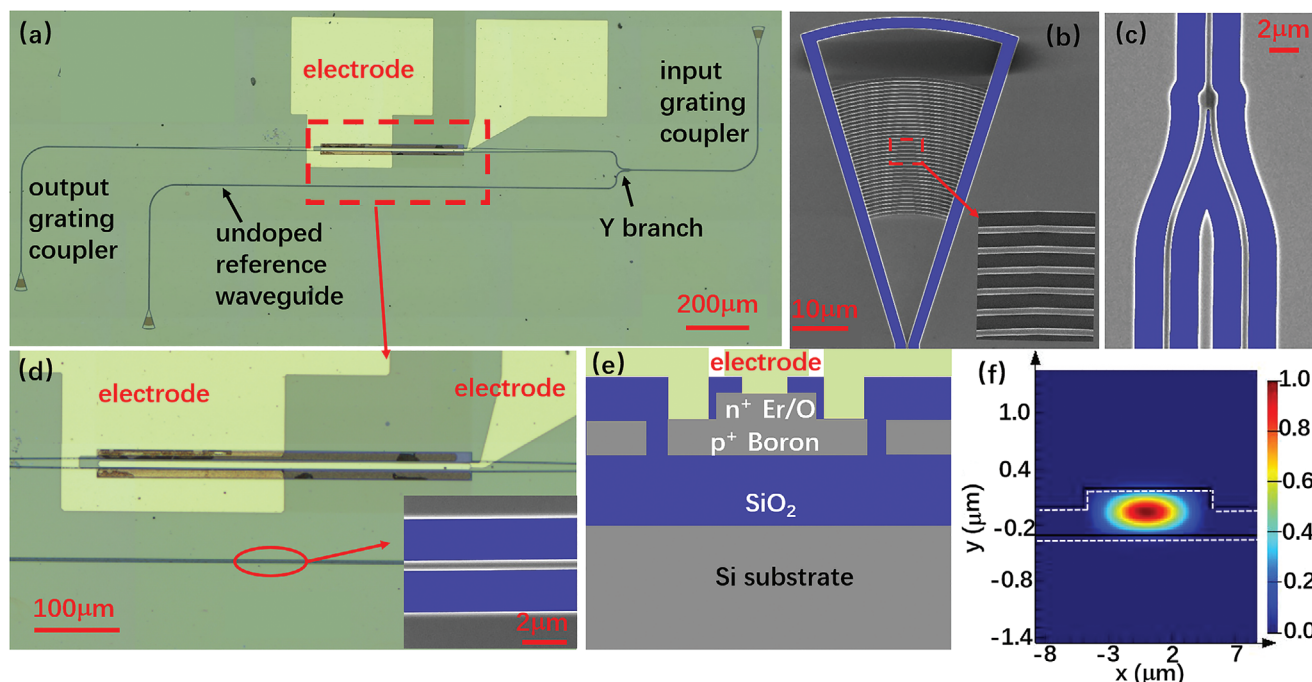


**Figure 1.** a) Optical microscope image of the Er/O doped silicon waveguide photodetector. b) False color SEM image of the grating coupler. c) False color SEM image of the Y branch. The blue color is SiO<sub>2</sub> and the grey color represents Si. d) Optical microscope image of the active region. Inset: SEM image of the silicon waveguide. e) Cross section of the rib waveguide photodetector. f) Calculated mode profile of the rib waveguide.

down at a rate of 1000 °C s<sup>-1</sup> by flushing with Helium gas that is cooled in liquid nitrogen (77 K). The dramatic cooling process suppresses the precipitation of Er/O composites as the Er/O composites dissolved in silicon at high temperature do not have enough time to precipitate. After the process, the Er/O doped Si is further made into a Si waveguide photodiode for the potential applications as integrated optic sensors<sup>[39,40]</sup> and integrated interferometric optical gyroscopes.<sup>[41,42]</sup>

## 2. Results and Discussion

The Er/O doped Si waveguide photodiodes were fabricated by first patterning the device layer (500 nm thick) of an silicon on insulator (SOI) wafer using the standard electron beam lithography and reactive ion etch. An optical microscopic image of the fabricated waveguide photodetector is shown in **Figure 1a**. Incident light is coupled from a source fiber into the waveguide through a grating coupler (top right) and splits equally into two parallel waveguides via a Y branch. The output light transmits into free space through the grating coupler at the left bottom and is picked up by a sense fiber. The scanning electron microscopic (SEM) false color images of the fabricated grating couplers and Y branch are shown in **Figure 1b,c**, respectively. To maximize the coupling efficiency, the grating coupler is designed to have a grating pitch of 728 nm, a duty cycle of 0.328 and an etch depth of 100 nm (out of the 500 nm thick device layer). The lower waveguide connecting to the Y branch (see **Figure 1a,d**) is an undoped 500 nm wide Si waveguide for reference. The upper waveguide expands to 10 μm wide where the Si rib waveguide is doped with erbium, oxygen, and boron ions to form a PN junction diode. The fabrication details are described

in the Experimental Section. A zoom-in optical microscopic image of the PN junction diode is shown in **Figure 1d**. The schematic cross-section of the rib waveguide photodetector is depicted in **Figure 1e**. The top 160 nm of the 500 nm thick device layer is doped with Er/O to form the highly doped n<sup>+</sup> region and the bottom layer is implanted with high energy boron ions to form the p<sup>+</sup> region. A DC process was employed to treat the sample, in which the sample was first inductively heated to 950 °C to activate all dopants and then rapidly cooled down to -125 °C in 5 s by flushing with liquid-nitrogen-cooled Helium gas. The dramatic cooling process suppresses the precipitation of Er/O composites, as a result of which the density of nonradiative recombination centers is significantly reduced. A lower density of nonradiative recombination centers will increase the optical sensitivity of Er-related defects. Optical simulations show that the fundamental mode of the rib waveguide is confined in the rib region (**Figure 1f**) where the implanted Er/O ions are located. This optical confinement will allow light at communication wavelength to be efficiently absorbed via Er-related defects so that the photoresponsivity is enhanced.

To quantitatively characterize the absorption efficiency of light at communication wavelength by Er/O doped silicon, we fabricated an array of Si waveguide with the Er/O doping region varying from 90 to 320 μm in length. Correspondingly, for both DC and RTA processed sample, the loss increases linearly with the length of the doped region (**Figure 2a**) at a light wavelength of 1550 nm, from which we found a loss of 92.5 dB mm<sup>-1</sup> for DC processed Er/O doped silicon waveguides and 129.4 dB mm<sup>-1</sup> for RTA treated sample. This loss dominantly comes from the absorption of photons via Er/O defects, because the transmission loss in the undoped silicon waveguide is only ≈5.46 dB mm<sup>-1</sup> (solid squares in **Figure 2a**).

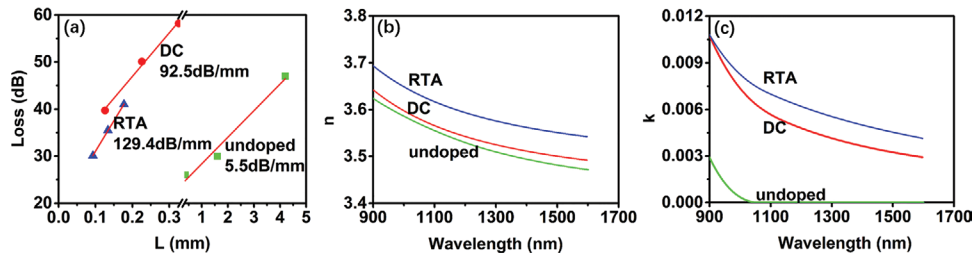


**Figure 2.** a) Transmission and absorption loss of the fabricated 500 nm-wide Si waveguide at 1550 nm. b) Real part of refractive index of the Er/O doped and undoped Si wafer. c) Imaginary part of refractive index of the Er/O doped and undoped Si wafer.

Analytically, the absorption loss is governed by the following equation Equation (1)<sup>[43]</sup>

$$\text{loss} = -20 \log_{10} (e^{-k2\pi/\lambda}) \quad (1)$$

where  $k$  is the imaginary part of refractive index and  $\lambda$  is the wavelength. The 92.5 and 129.4 dB mm<sup>-1</sup> loss correspond to a  $k$  value of  $\approx 0.0026$  and 0.0037, respectively. To verify these values, we prepared two single crystalline silicon wafers that were implanted with Er/O at the same doping concentration and ion implantation energy as the samples in Figure 2a. One of the samples was treated with the deep cooling process and the other sample was treated with standard RTA process. The refractive index of the Er/O doped silicon wafer and the undoped wafer were measured by ellipsometry. The real part  $n$  and imaginary part  $k$  of the refractive index for the Er/O doped and undoped Si wafer are shown in Figure 2b,c, respectively. Both  $n$  and  $k$  of the Er/O doped wafer are increased in comparison with the undoped silicon wafer while the RTA processed wafer has a higher  $n$  and  $k$  value than the DC treated wafer. The RTA processed sample has a higher  $k$  value likely because the sample has a higher concentration of defects. It is straightforward that a higher concentration of defects leads to a more lossy material, therefore a higher  $k$  value. For the  $n$  value, semiconductor materials with a lower electron concentration will have a larger  $n$  value.<sup>[44]</sup> Our RTA processed Si wafer has a lower electrical conductivity than DC processed Si wafer. As a result, the  $n$  value is also higher than the DC processed Si wafer. The imaginary part  $k$  at 1550 nm measured by ellipsometry is about 0.003 for DC treated sample and 0.0043 for RTA treated sample. Note that the estimated imaginary value of  $k$  of ellipsometric results

from both DC- and RTA-treated samples are slightly higher than the values calculated from loss measurement of the corresponding waveguides. It is probably because the ellipsometric measurements reflect the index of materials near the silicon surface where the Er/O impurities have a maximum concentration. In contrast, the loss measurements accounts for the averaged effect of all Er/O impurities.

**Figure 3a** shows the current versus voltage ( $I$ - $V$ ) characteristics of the fabricated Er/O doped waveguide photodetector that was treated with the deep cooling process. The PN junction diode exhibits a reasonably good rectifying behavior with the leakage current four orders of magnitude smaller than the forward current. The ideality factor of the PN junction diode at small injection is approximately equal to 2 (inset of Figure 3a), indicating that electrons and holes at forward bias dominantly recombine through defects (likely Er-related) in Si bandgap. Under a reverse bias of -2 V, a relatively large dark current density ( $\approx 3$  mA cm<sup>-2</sup> at room temperature in Figure 3b) is observed via these defects by thermal generation. Based on the theory of carrier generation-recombination via defects in semiconductors, we derived the dark current density that is dependent on the defect concentration and energy level as shown in Equation (2)

$$J_{\text{dark}} = qW_{\text{dep}}C_pN_tN_v \exp\left(-\frac{E_g}{kT}\right) \exp\left(\frac{E_c - E_t}{kT}\right) \quad (2)$$

in which  $q$  is the unit of charge,  $W_{\text{dep}}$  is the depletion region width,  $C_p$  is the hole capture cross-section,  $N_t$  is the concentration of defects,  $N_v$  is the carrier concentration associated with the valence band,  $E_g$  is the bandgap of semiconductor (Si),  $E_c$

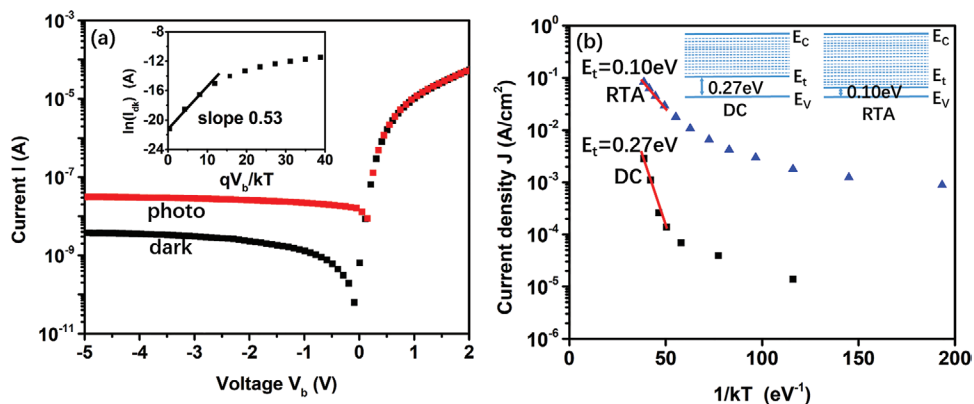


**Figure 3.** a) Photo and dark  $I$ - $V$  curves of the fabricated Er doped pin photodetector. Inset:  $\ln(I_{\text{ph}})$  as a function of  $qV_b/kT$ . b) Temperature dependent dark current density of the deep cooling and RTA processed samples.

is the conduction band edge, and  $E_t$  is the defect energy level. According to Equation (2), the dark current density is highly dependent on temperature. For this reason, we measured the dark current density as a function of temperature for both DC and RTA processed samples as shown in Figure 3b. In comparison with the RTA sample, the dark current density of the DC sample is two orders of magnitude smaller, indicating that the deep cooling process reduces the density of Er-rated defects by two orders of magnitude. This observation is consistent with our recent finding that photoluminescence from the deep-cooling-processed samples is two orders of magnitude stronger than the RTA-processed ones.<sup>[31]</sup> In Figure 3b, the dark current density for both samples first drops exponentially due to the dominance of the exponential terms in Equation (2). The current later levels off at lower temperature due to the nonexponential term in Equation (2) that is a power function of temperature  $T$ . From the exponential dependence, we found that the defect energy levels are located 0.27 and 0.10 eV ( $= E_t - E_v$ ) above the Si valence band for the DC and RTA processed sample, respectively (see Figure 3b). This means that electrons only need to overcome an energy gap of 0.27 or 0.10 eV to create the observed dark current. However, the bandgap of Si is 1.12 eV. If the defects form a single energy level, there will be still a large energy gap (0.85 or 1.02 eV) for electrons to thermally excite from the defect energy level  $E_t$  to the conduction band edge. The Arrhenius plot in Figure 3b does not support this assumption of a single defect energy level. A possible scenario is that the Er/O related defects may have formed a quasicontinuous band from  $E_t$  to the Si conduction band edge, as shown in the inset of Figure 3b. This scenario is consistent with our recent observations that the PL spectrum from the Er/O doped Si has a surprisingly wide broad emission band (0.6–1.1 eV) in addition to the widely reported strong  $\text{Er}^{3+}$  emission peak at 1536 nm.<sup>[45]</sup> Similar quasicontinuous band was also observed in sulfur-doped silicon.<sup>[46]</sup>

No detectable photocurrent was observed for the sample treated by RTA even when the light at the highest possible intensity is coupled from our tunable laser (Agilent 81640A) into the detector waveguide (upper waveguide in Figure 1a). In contrast, the photodetector treated by the deep cooling process exhibits a relatively large photocurrent at reverse bias (Figure 4a). To find out photoresponsivity of the device, we need to calibrate the light power reaching the Er/O photodetector. Since the incident light splits equally into the reference and detector waveguide via

the Y branch, the power reaching the Er/O photodetector can be calculated from the output power at the undoped reference end after taking into account the coupling loss and the Si waveguide transmission loss. Figure 4a shows the power dependent photocurrent and corresponding photoresponsivity of the Er/O doped photodetector that is treated with the deep cooling process. It is surprising to see that the photocurrent increases sublinearly as the light power ramps up, in contrast with the linear increase of photocurrent in standard PIN photo diodes. This may be caused by the relatively low density of Er-related defect states that limit the absorption efficiency of photons when the flux is high. As a result, the photoresponsivity (at 1570 nm and bias voltage of  $-1$  V) increases (up to  $3 \text{ mA W}^{-1}$ ) as the light power reduces. Figure 4b shows the spectral responsivity of a  $50 \mu\text{m}$  long Er photodetector. The spectrum is not uniform mainly due to the non-uniformity of the power (inset in Figure 4b) that affects the photoresponsivity (Figure 4a). The maximum photoresponsivity reaches  $100 \text{ mA W}^{-1}$  at 1510 nm and bias voltage of  $-5$  V, which outperforms the previously reported Er:Si by RTA,<sup>[28]</sup> Si:Ag photodiodes,<sup>[24]</sup> Si:Ag photodiodes,<sup>[27]</sup> and Si:Zn photodiodes<sup>[17]</sup> in literatures. Our recent studies show that the activation rate of Er ions is closely related with Er/O doping concentration and deep cooling condition (annealing temperature, annealing time, and cooling time). By carefully optimizing these parameters, the responsivity of the Er/O doped Si photodiode can be further improved. Additional experiments show that the spectral response can extend up to  $\lambda = 3.5 \mu\text{m}$  (data not shown here). This is in line with the hypothetical quasicontinuous defect band in the bandgap of silicon and the broad PL emission from the Er/O doped Si that were mentioned above.

Transient current measurement (diagram in Supporting Information) shows fast and high photoresponses when the light is turn on and turn off periodically, as shown in Figure 5a. The 1550 nm light signal is modulated by an acousto-optic (AO) modulator (CETC SGT200-02-N-1D) with a modulation frequency from 200 Hz to 100 kHz. The modulated light signal is coupled to the SOI waveguide through the grating coupler. The Er/O doped Si PN photodetector is reversely biased and the photocurrent is picked up by a lock-in amplifier SR830. The measured 3dB bandwidth of our  $100 \mu\text{m}$  long Er/O photodetector is  $\approx 30$  kHz (Figure 5b). According to the calculation, the junction capacitance of the  $100 \mu\text{m}$  long Er/O photodetector is about 6.18 pF (see the Supporting Information for details). From the forward  $I$ - $V$  curve of our Er/O doped Si photodiode,

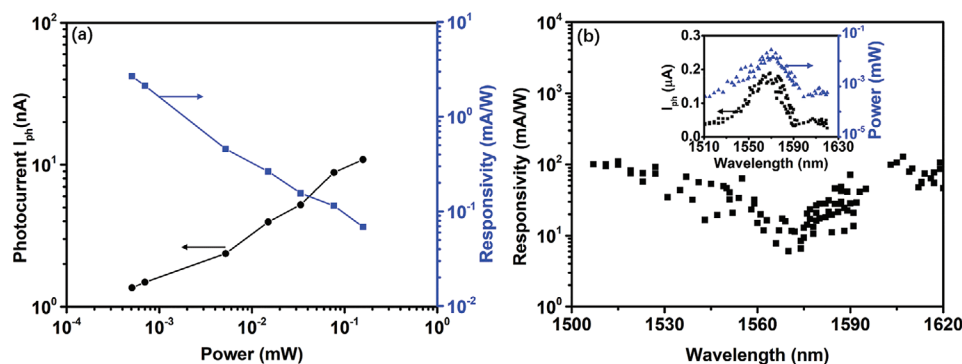


**Figure 4.** a) Photocurrent and responsivity at 1570 nm as a function of power at bias voltage of  $-1$  V. b) Responsivity spectrum of a  $50 \mu\text{m}$ -long Er/O doped photodetector under  $-5$  V bias. Inset: Photocurrent and power spectra.

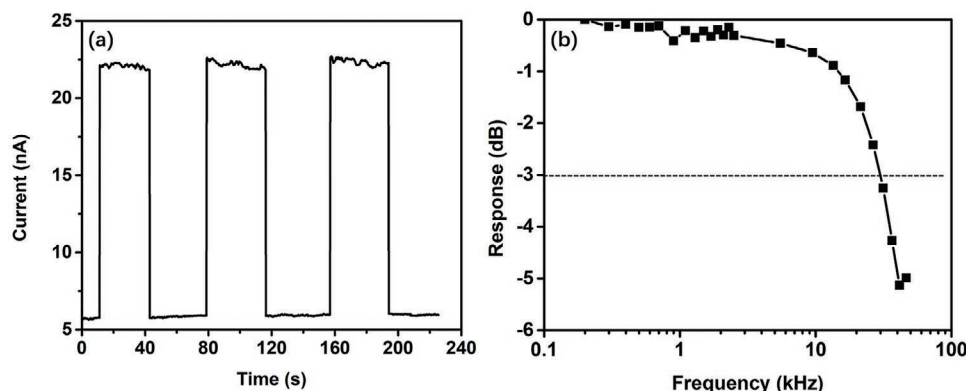


**Figure 5.** a) Transient current response of the Er/O doped photodetector at bias voltage of  $-1V$ . b) Frequency response of the Er/O doped photodetector at bias voltage  $-1V$ .

the series resistance  $R_s$  is around  $4 \times 10^4 \Omega$ . With a junction capacitance of 6.18 pF, the capacitance charging time is  $\tau_c = R_s C = 2.4 \times 10^{-7}$  s. If the frequency is dominated by the

capacitance, the 3dB bandwidth will be  $f_c = \frac{1}{2\pi\tau_c} = 660$  kHz,

which is much higher than the 30 kHz bandwidth of our Er/O doped Si waveguide photodiode. Therefore, it is concluded that the frequency response of the DC processed Er/O doped Si waveguide photodiode is dominated by the slow back-transfer rate. The back-transfer rate of RTA processed Er/O doped Si wafer is reported to be  $\approx 1.7 \times 10^6$  s $^{-1}$  (corresponding to back-transfer time  $5.9 \times 10^{-7}$  s).<sup>[29]</sup> The DC processed Er/O doped Si wafer will have a much longer back-transfer time since its photoluminescence efficiency is largely enhanced.<sup>[31]</sup> The DC processed Er/O doped Si waveguide photodiode may have a back transfer time possibly up to  $5 \times 10^{-6}$  s, which leads to a

cutoff frequency  $f_{bt} = \frac{1}{2\pi\tau_{bt}} = \frac{1}{2 \times 3.14 \times 5 \times 10^{-6}} = 30$  kHz.

Although 30 kHz bandwidth is not enough for fiber communication system, the Er/O photodetectors may find applications as integrated optic sensors.<sup>[39]</sup> Waveguide-based optical sensors are used in a variety of applications such as label-free detection of chemical<sup>[40]</sup> or integrated interferometric optical gyroscopes for navigation,<sup>[41,42]</sup> in which high frequency is not a critical factor.

### 3. Conclusion

In this work, we applied a DC thermal treatment on Er/O doped SOI wafer as an alternative to the traditional RTA treatment. The DC treated Er/O doped Si waveguide showed a reduced absorption loss, as further confirmed by the ellipsometric measurements of  $n$  and  $k$ , due to the reduced defect concentration by the dramatically cooling process of DC. The Er/O doped Si wafers were further doped with B to form vertical PN junctions and patterned into rib waveguides. The rib waveguide photodiode showed a decreased dark current density and a significantly enhanced photoresponsivity (up to 100 mA W $^{-1}$  at 1510 nm) at communication wavelength. Besides, a 3dB band-

width around 30 kHz is achieved on the Er/O doped Si rib waveguide photodetector. With the advantages of high responsiveness, low-cost and CMOS-compatible process, it is promising for the monolithic integrated IR photodetector application.

### 4. Experimental Section

**Device Fabrication:** The microfabrication process started with an SOI wafer with a 500 nm thick device layer and 2  $\mu$ m BOX layer. Photolithography was performed to allow selective doping in the active region. Boron was ion implanted with energy of 110 keV and dosage of  $7 \times 10^{14}$  cm $^{-2}$ . Er was ion implanted with energy of 200 keV and dosage of  $4 \times 10^{15}$  cm $^{-2}$ . O was incorporated with energy of 32 keV and dosage of  $1 \times 10^{16}$  cm $^{-2}$ . Electron beam lithography and reactive ion etch were performed to form the waveguide pattern. The Er/O doped rib waveguide was etched 200 nm thickness. The above processes were performed again to form the grating coupler. 200 nm thick SiO $_2$  was sputtered as the isolating layer. After DC, electrodes were patterned and deposited by photolithography and thermal evaporation. To reduce the absorption by metal electrodes, ITO was applied as the contact material for Er/O doped region. The large electrode pads and contact material for Boron doped region were Ti/Au.

**Deep Cooling:** The DC process was performed in an upgraded dilatometer (DIL 805A, TA Instruments, see Figure S1, Supporting Information). The Er/O doped Si samples were first heated at 950  $^{\circ}$ C for 5 min by means of copper coil-based electromagnetic heating and then cooled down to room temperature in 5 s by a flush of high purity Helium (99.999%) gas cooled in liquid nitrogen (77 K). Compared to traditional RTA process, the deep cooling method has a much larger cooling rate (up to 1000  $^{\circ}$ C s $^{-1}$ ).

### Supporting Information

Supporting Information is available from the Wiley Online Library or from the author.

### Acknowledgements

The work was financially supported by the special-key project of Innovation Program of Shanghai Municipal Education Commission (No. 2019-07-00-02-E00075), China Postdoctoral Science Foundation (Nos. 2019M661506) and National Science Foundation of China (NSFC) (Nos. 61874072 and 61904102). The devices were fabricated at the center for Advanced Electronic Materials and Devices (AEMD), Shanghai Jiao Tong University.

## Conflict of Interest

The authors declare no conflict of interest.

## Data Availability Statement

The data that support the findings of this study are available from the corresponding author upon reasonable request.

## Keywords

communication wavelength, deep cooling, defect, erbium doping, silicon waveguide photodetectors

Received: February 4, 2021  
Revised: March 16, 2021  
Published online: May 31, 2021

- [1] C. L. Tan, H. Mohseni, *Nanophotonics* **2018**, 7, 169.
- [2] A. Rogalski, *Opto-Electronics Review* **2012**, 20.
- [3] A. Rogalski, *Infrared Phys. Technol.* **2002**, 43, 187.
- [4] X. Liu, B. Kuyken, G. Roelkens, R. Baets, R. M. Osgood, W. M. J. Green, *Nat. Photonics* **2012**, 6, 667.
- [5] W. Zheng, L. Jia, F. Huang, *iScience* **2020**, 23, 101145.
- [6] W. Zheng, R. Lin, J. Ran, Z. Zhang, X. Ji, F. Huang, *ACS Nano* **2018**, 12, 425.
- [7] W. Zheng, F. Huang, R. Zheng, H. Wu, *Adv. Mater.* **2015**, 27, 3921.
- [8] S. Liao, N. N. Feng, D. Feng, P. Dong, R. Shafiiha, C. C. Kung, H. Liang, W. Qian, Y. Liu, J. Fong, J. E. Cunningham, Y. Luo, M. Asghari, *Opt. Express* **2011**, 19, 10967.
- [9] J. Wu, Q. Jiang, S. Chen, M. Tang, Y. I. Mazur, Y. Maidaniuk, M. Benamara, M. P. Semtsiv, W. T. Masselink, K. A. Sablon, G. J. Salamo, H. Liu, *ACS Photonics* **2016**, 3, 749.
- [10] S. Mauthe, Y. Baumgartner, M. Sousa, Q. Ding, M. D. Rossell, A. Schenk, L. Czornomaz, K. E. Moselund, *Nat. Commun.* **2020**, 11, 4565.
- [11] T. Yin, R. Cohen, M. M. Morse, G. Sarid, Y. Chetrit, D. Rubin, M. J. Paniccia, *Opt. Express* **2007**, 15, 13965.
- [12] L. Vivien, J. Osmond, J. M. Fedeli, D. Marris-Morini, P. Crozat, J. F. Damlencourt, E. Cassan, Y. Lecunff, S. Laval, *Opt. Express* **2009**, 17, 6252.
- [13] M. Casalino, G. Coppola, M. Iodice, I. Rendina, L. Sirleto, *Sensors* **2010**, 10, 10571.
- [14] A. Rickman, *Nat. Photonics* **2014**, 8, 579.
- [15] G. Masini, L. Colace, G. Assanto, *Mater. Sci. Eng., B* **2002**, 89, 2.
- [16] L. Pavesi, *J. Phys.: Condens. Matter* **2003**, 15, R1169.
- [17] R. R. Grote, B. Souhan, N. Ophir, J. B. Driscoll, K. Bergman, H. Bahkru, W. M. J. Green, R. M. Osgood, *Optica* **2014**, 1, 264.
- [18] Y. Li, W. Zheng, F. Huang, *Photonix* **2020**, 1, 15.
- [19] S. Hu, P. Han, S. Wang, X. Mao, X. Li, L. Gao, *Semicond. Sci. Technol.* **2012**, 27, 102002.
- [20] J. E. Carey, C. H. Crouch, M. Shen, E. Mazur, *Opt. Lett.* **2005**, 30, 1773.
- [21] T. G. Kim, J. M. Warrender, M. J. Aziz, *Appl. Phys. Lett.* **2006**, 88, 241902.
- [22] B. P. Bob, A. Kohn, S. Charnvanichborikarn, J. M. Warrender, I. Umezu, M. Tabbal, J. S. Williams, M. J. Aziz, *J. Appl. Phys.* **2010**, 107, 123506.
- [23] M. J. Smith, M.-J. Sher, B. Franta, Y.-T. Lin, E. Mazur, S. Gradečak, *J. Appl. Phys.* **2012**, 112, 083518.
- [24] J. P. Mailoa, A. J. Akey, C. B. Simmons, D. Hutchinson, J. Mathews, J. T. Sullivan, D. Recht, M. T. Winkler, J. S. Williams, J. M. Warrender, P. D. Persans, M. J. Aziz, T. Buonassisi, *Nat. Commun.* **2014**, 5, .
- [25] K. Mallik, R. J. Falster, P. R. Wilshaw, *Semicond. Sci. Technol.* **2003**, 18, 517.
- [26] K. Graff, *Metal Impurities in Silicon-Device Fabrication*, Vol. 24, Springer Science & Business Media, Berlin **2013**.
- [27] X. Qiu, Z. Wang, X. Hou, X. Yu, D. Yang, *Photonics Research* **2019**, 351, 7.
- [28] P. G. Kik, A. Polman, S. Libertino, S. Coffa, *J. Lightwave Technol.* **2002**, 20, 862.
- [29] N. Hamelin, P. G. Kik, J. F. Suyver, K. Kikoin, A. Polman, A. Schönecker, F. W. Saris, *J. Appl. Phys.* **2000**, 88, 5381.
- [30] A. J. Kenyon, S. S. Bhamber, C. W. Pitt, *Mater. Sci. Eng., B* **2003**, 105, 230.
- [31] H. Wen, J. He, J. Hong, S. Jin, Z. Xu, H. Zhu, J. Liu, G. Sha, F. Yue, Y. Dan, *Adv. Opt. Mater.* **2020**, 8, 2000720.
- [32] A. J. Kenyon, *Semicond. Sci. Technol.* **2005**, 20, R65.
- [33] Y. Yin, K. Sun, W. J. Xu, G. Z. Ran, G. G. Qin, S. M. Wang, C. Q. Wang, *J. Phys.: Condens. Matter* **2008**, 21, 012204.
- [34] B. Zheng, J. Michel, F. Y. G. Ren, L. C. Kimerling, D. C. Jacobson, J. M. Poate, *Appl. Phys. Lett.* **1994**, 64, 2842.
- [35] M. A. Lourenco, M. M. Milosevic, A. Gorin, R. M. Gwilliam, K. P. Homewood, *Sci. Rep.* **2016**, 5, 37501.
- [36] F. Priolo, G. Franzò, S. Coffa, A. Carnera, *Phys. Rev. B* **1998**, 57, 4443.
- [37] V. P. Kuznetsov, R. A. Rubtsova, V. N. Shabanov, A. P. Kasatkin, S. V. Sedova, G. A. Maksimov, Z. F. Krasil'nik, E. V. Demidov, *Phys. Solid State* **2005**, 47, 102.
- [38] S. Scalese, G. Franzò, S. Mirabella, M. Re, A. Terrasi, F. Priolo, E. Rimini, C. Spinella, A. Carnera, *J. Appl. Phys.* **2000**, 88, 4091.
- [39] L. S. Grattan, B. T. Meggit, *Optical Fiber Sensor Technology Chemical and Environmental Sensing Springe*, Vol. 4, Springer, Berlin **1998**, pp. 113–132.
- [40] R. E. Kunz, K. Cottier, *Anal. Bioanal. Chem.* **2006**, 384, 180.
- [41] B. Wu, Y. Yu, J. Xiong, X. Zhang, *Sci. Rep.* **2018**, 8, 8766.
- [42] D. Liu, H. Li, X. Wang, H. Liu, P. Ni, N. Liu, L. Feng, *Opt. Express* **2020**, 28, 15718.
- [43] L. Chrostowski, M. Hochberg, *Silicon Photonics Design: From Devices to Systems*, Cambridge University Press, Cambridge **2015**.
- [44] R. Soref, B. Bennett, *IEEE J. Quantum Electron.* **1987**, 23, 123.
- [45] J. Hong, H. Wen, J. He, J. Liu, Y. Dan, J. W. Tamm, F. Yue, J. Chu, C. Duan, *Photonics Research*, **2021**, unpublished, <https://doi.org/10.1364/PRJ.417090>.
- [46] M. T. Winkler, D. Recht, M.-J. Sher, A. J. Said, E. Mazur, M. J. Aziz, *Phys. Rev. Lett.* **2011**, 106, 178701.